

Optical floating zone growth of high-quality Cu_2MnAl single crystals

A. Neubauer^{a,b,*}, F. Jonietz^a, M. Meven^c, R. Georgii^c, G. Brandl^c, G. Behr^d,
P. Böni^a, C. Pfeiderer^a

^a*Physik Department E21, Technische Universität München, James Franck Straße, 85748 Garching, Germany*

^b*Bundesanstalt für Materialforschung und -prüfung, 12205 Berlin, Germany*

^c*Forschungsneutronenquelle Heinz Maier Leibnitz (FRM II), Lichtenbergstr. 1, 85748 Garching, Germany*

^d*IFW Dresden, PF 270116, D-01171, Dresden, Germany*

Abstract

We report the growth of large single-crystals of Cu_2MnAl , a ferromagnetic Heusler compound suitable for polarizing neutron monochromators, by means of optical floating zone under ultra-high vacuum compatible conditions. Unlike Bridgman or Czochralsky grown Cu_2MnAl , our floating zone grown single-crystals show highly reproducible magnetic properties and an excellent crystal quality with a narrow and homogeneous mosaic spread as examined by neutron diffraction. An investigation of the polarizing properties in neutron scattering suggests a high polarization efficiency, limited by the relatively small sample dimensions studied. Our study identifies optical floating zone under ultra-high vacuum compatible conditions as a highly reproducible method to grow high-quality single-crystals of Cu_2MnAl .

Keywords: single crystal growth, optical floating zone, polarized neutron scattering, polarizing monochromator, mosaicity

1. Introduction

Heusler compounds exhibit a remarkably wide variety of different electronic ground states ranging from simple metallic, over semiconducting to insulating behavior including recent theoretical proposals, which suggest the possibility of topological insulators [1]. Heusler compounds also stabilize various forms of electronic order including half-metallic ferromagnetism and superconductivity [2]. This has motivated great efforts to exploit the wide range of ground states by combining different materials in 'all-Heusler devices' [3, 4, 5]. Based on these activities the preparation of high-quality single crystals of Heusler compounds is of considerable general interest.

In this paper we address the properties of Cu_2MnAl , the first compound made of non-ferromagnetic elements, in which Fritz Heusler discovered ferromagnetism in 1903 [6]. Cu_2MnAl orders ferromagnetically at $T_C = 622$ K

*Corresponding author
Preprint submitted to Elsevier
Email address: andreas.neubauer@bam.de (A. Neubauer)

27 with an ordered magnetic moment of $3.6 \mu_B$ per formula unit [7]. Cu_2MnAl is
28 mostly known for its use in polarizing monochromators for neutron scattering
29 techniques[8].

30 Scattering off the (111) Bragg peak is thereby typically used to generate
31 a monochromatic polarized neutron beam [9, 10]. In turn, the main challenge
32 in the preparation of monochromators for polarized neutron scattering using
33 Cu_2MnAl Heusler single crystals consists in the growth of large and homoge-
34 neous crystals with a well defined mosaic spread. A mosaic spread in the range
35 of $0.2^\circ - 1^\circ$ is desirable in order to match the divergences of the neutron beam,
36 and hence obtain large intensities [11]. As the main problem previous studies
37 established that Cu_2MnAl single-crystals prepared by the Bridgman technique
38 are characterized by very large, uncontrolled anisotropies of the mosaic distri-
39 bution depending on the growth direction[12, 13]. Due to this sensitivity of the
40 crystal quality on the growth conditions less than 50% of the crystals are suitable
41 for monochromators. Moreover, it implies the need for very careful screening of
42 the samples to identify sections of the ingots with suitable properties. To high-
43 light the need for advances in the synthesis of Heusler single crystals one has
44 to consider that modern focusing and double-focusing monochromator devices
45 often need in the order of 100 crystals or more.

46 In this paper we report the growth of single crystals of Cu_2MnAl by means of
47 optical floating zone. Altogether eight single crystals were grown, two in a verti-
48 cal double ellipsoid image furnace at IFW Dresden and six in a UHV-compatible
49 four-mirror image furnace at TU Munich [14]. The UHV compatible conditions
50 were found to promote stable growth conditions, resulting in a mono-crystalline
51 state over the entire cross-section of the rods. The magnetic properties and
52 the crystal structure of four of those six crystals were investigated in detail.
53 In addition, a systematic study of the polarizing properties of these crystals in
54 neutron scattering was carried out at the diffractometer MIRA at FRMII. To
55 assess the properties of the floating zone grown crystals they were compared
56 with commercial Bridgman grown Cu_2MnAl crystals investigated in the same
57 way. As our main result we find that optical floating zone growth under UHV
58 compatible conditions is ideally suited to grow high quality single crystals of
59 Cu_2MnAl with a small isotropic mosaic spread.

60 2. Single crystal growth

61 Single-crystal growth of Cu_2MnAl is challenging, as the detailed ternary
62 phase diagram of the Cu-Mn-Al system has not been reported. Yet, a series
63 of publications suggests that Cu_2MnAl is congruently melting and crystallizes
64 around 1125 K in the cubic $L2_1$ Heusler structure [7, 12, 15, 16, 17, 18]. This
65 so-called β -phase appears to be metastable and does not exist in the equi-
66 librium phase diagram at room temperature. Below around 923 K Cu_2MnAl
67 presumably decomposes in a solid state reaction into Cu_9Al_4 , $\text{Cu}_3\text{Mn}_2\text{Al}$, and
68 β -Mn phases. However, since the transformation kinetics of this solid state re-
69 action slows down dramatically well below 923 K, it has been possible to prepare
70 Cu_2MnAl in a quasi-stable state at room temperature when cooling samples

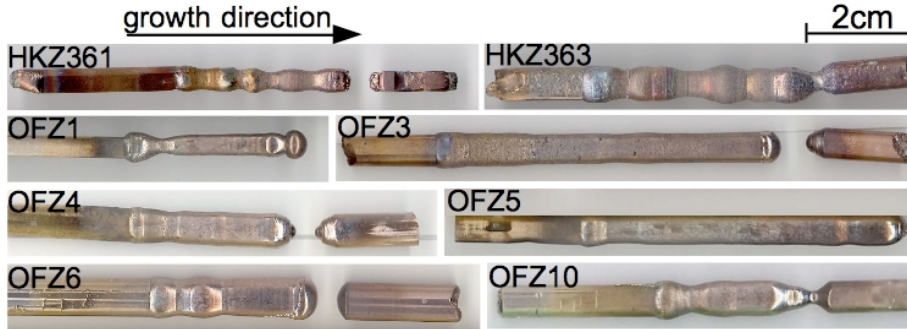


Figure 1: The Cu_2MnAl crystals grown by optical floating zone for this study. HKZ361 and HKZ363 were grown at the IFW in Dresden. An abundance of oxide contamination disturbed stable growth conditions, leading to repeated separations of the zone during crystal growth. The inhomogeneous shape of the crystals (swellings and contractions) and the gray and brown staining are the visible results. In comparison, the Cu_2MnAl crystals OFZ1, OFZ3, OFZ4, OFZ5, OFZ6, and OFZ10 were grown with a UHV-compatible image furnace at the TUM[14], leading to stable growth conditions. A more homogeneous shape of the rods and a reduced staining are the visible results. The length scale shown in the top right applies to all crystals.

71 sufficiently fast. The hidden agenda in our study was hence, whether the tem-
 72 perature gradient along the sample in optical-float zoning may drive such a
 73 decomposition.

74 Shown in Fig. 1 are the eight crystals grown for our study by vertical floating
 75 zone. Two crystals were grown in a vertical double ellipsoid image furnace
 76 (model URN-2-ZM, MPEI, Moscow) at the IFW in Dresden. They are labeled
 77 HKZ361 and HKZ363. The other six crystals were grown in a refurbished UHV-
 78 compatible four-mirror image furnace (model CSI FZ-T-10000-H-III-VPS) at
 79 the Technical University in Munich [14]. They are labeled OFZ1, OFZ3, OFZ4,
 80 OFZ5, OFZ6, and OFZ10.

81 Rectangular bars with a rectangular cross-section of $4 \times 4 \text{ mm}^2$ prepared
 82 from stoichiometric Bridgman grown single crystals were used as starting rods
 83 for the floating zone growth of HKZ361 and OFZ1. For all other crystals cylin-
 84 dric seed and feed rods of stoichiometric Cu_2MnAl polycrystals with a diameter
 85 of 6 mm were prepared in bespoke rod-casting furnace at the IFW Dresden
 86 and TUM, respectively [19]. The rod-casting furnace at TUM was especially
 87 designed to offer UHV-compatible conditions [20, 21, 22].

88 Crystals HKZ361 and HKZ363 were grown at a rate of 15 mm/h and with
 89 a counter-rotation of 40 rpm (seed) and 25 rpm (feed). Growth took place in
 90 a high purity flowing Argon gas environment (6-10l/h) at $p \sim 1.1 \text{ bar}$. An
 91 abundance of oxide contamination flowing on the molten zone disturbed a stable
 92 growth process for both crystals. Attrition of oxide layers led to a shaking of
 93 the zone that resulted in repeated separations of the zone during the growth
 94 process. The resulting inhomogeneous shape of the crystals and the strong
 95 contamination with oxide on the outside of HKZ361 and HKZ363 (indicated by
 96 the grey and brown staining) can be seen in Fig. 1.

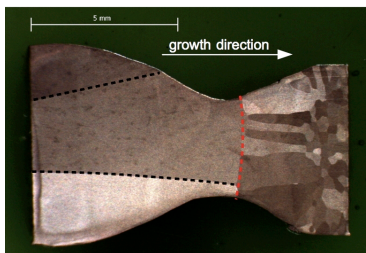


Figure 2: (a) Final zone of HKZ363. Three large grains can be clearly identified on the left hand side of the interface (indicated by the horizontal dashed lines). These grains are separated by a slightly convex growth interface (see vertical dashed line) from the poly-crystalline feed rod, where large grains already form probably due to annealing. The surfaces was polished and etched with Marble reagent ($2.5 \text{ g CuSO}_4 + 30 \text{ cm}^3 \text{ HCl} + 25 \text{ cm}^3 \text{ H}_2\text{O}$) in order to highlight grain structures.

97 Large single crystal grains formed in all crystals as illustrated in Fig. 2. The
 98 image shows the quenched last zone of HKZ363. The surface was etched with
 99 Marble reagent ($2.5 \text{ g CuSO}_4 + 30 \text{ cm}^3 \text{ HCl} + 25 \text{ cm}^3 \text{ H}_2\text{O}$) for a better visibility
 100 of the grain structure. The growth direction is from the left to the right. In
 101 the crystal three grains can be identified with the grain at the center expanding
 102 in size. A slightly convex growth interface (marked by the vertical dashed line)
 103 separates the crystal that was grown from the poly-crystalline structure of the
 104 feed rod. In the poly-crystalline feed large grains already formed in the vicinity
 105 of the growth interface due to annealing. EDX investigation of the surface
 106 showed a stoichiometric Cu_2MnAl composition with no indication of secondary
 107 phases. These findings are consistent with earlier reports of Cu_2MnAl as a
 108 congruently melting compound that shows a strong trend to crystallize in a
 109 mono-crystalline state.

110 Crystals OFZ1, OFZ3, OFZ4, OFZ5, and OFZ6 were grown in the UHV-
 111 compatible image furnace at TUM at growth rates in the range 10-12 mm/h.
 112 In contrast, for OFZ10 the growth rate was increased from 5 mm/h to 10 mm/h
 113 during the growth (we return to this issue later). In each growth process the feed
 114 and seed rod were counter-rotating with 10 rpm and 30 rpm, respectively. Prior
 115 to each growth process the image furnace was carefully baked (10^{-8} mbar) and
 116 filled with 6N Argon gas, that was additionally purified with a getter furnace.
 117 Each growth process took place in a static Argon atmosphere of $p \sim 1.5$ bar. A
 118 strong reduction of the oxide layers floating on the molten zone was observed in
 119 comparison to the crystals grown in the non-UHV compatible furnace at IFW
 120 Dresden. This is clearly illustrated by the difference in surface contamination
 121 shown in Fig. 1. For the high-purity environment a stable molten zone formed
 122 readily during the whole growth process. We attribute the complete grain se-
 123 lection process, that resulted in a mono-crystalline structure across the entire
 124 cross section of the rod for all crystals grown in UHV-compatible image furnace
 125 at TUM to this improved stability of the zone.

126 For studies of the magnetization and neutron scattering large single-crystalline



Figure 3: (a) Single-crystalline Cu_2MnAl crystals investigated in detail. No preferred growth direction of the crystal structure could be identified.

127 samples were prepared from OFZ3, OFZ5, OFZ6 and OFZ10, as shown in Fig. 3.
 128 Single-crystallinity of the samples was at first established with a light micro-
 129 scope and by means of x-ray Laue diffraction. The orientation of the crystal
 130 structure with respect to the growth direction was determined by means of x-
 131 ray Laue diffraction. A different crystal orientation was found for each crystal.
 132 Since poly-crystalline rods rather than oriented crystals were used as seed rods
 133 in each growth process, this means that no preferred growth direction could be
 134 identified. In turn, this suggests that oriented seed crystals may allow to grow
 135 cylindrical single crystals of arbitrary crystallographic orientation.

136 3. Magnetization

137 The ferromagnetic properties of the Cu_2MnAl single-crystals grown served
 138 as first test of the sample quality. In order to avoid systematic errors due to
 139 demagnetizing effects in Cu_2MnAl [10] and to be able to quantitatively compare
 140 the magnetic properties, oriented samples of the same dimensions were prepared
 141 from OFZ3, OFZ5, OFZ6, OFZ10 and from a Bridgman grown single crystal
 142 (BM). The samples were cut in a rectangular parallelepiped $5 \times 2.5 \times 2 \text{ mm}^3$ (cf.
 143 Fig. 8) with the flat front surface being a (111) crystallographic plane and the
 144 small bottom surface a (110) plane.

145 All five samples were measured in a vibrating sample magnetometer (VSM)
 146 with the magnetic field parallel to the long axis of the parallelepiped, i.e., the
 147 configuration that minimizes the demagnetizing effects. Figs. 4 (a) and (b) show
 148 the field dependent magnetization at 4 K and 300 K for fields up to 9 T and for
 149 low fields, respectively. At high fields and 4 K the magnetization saturates for
 150 all samples at $m \sim 3.6 \mu_B/\text{f.u.}$. At 300 K the magnetization saturates for all
 151 samples at $m \sim 3.2 \mu_B/\text{f.u.}$. Both values are in excellent agreement with the
 152 literature [7]. At low fields the magnetization shows a linear slope followed by
 153 the onset of saturation at 90 mT for both temperatures and all samples. No
 154 evidence suggesting hysteretic behavior is observed in any of the samples. The
 155 magnetic moments of the samples differ by less than 3%. Hence, the magnetic
 156 properties of the floating zone grown crystals are in excellent agreement with
 157 respect to each other and as compared with the Bridgman grown sample. This
 158 establishes highly reproducible ferromagnetic properties of the floating zone
 159 grown crystals.

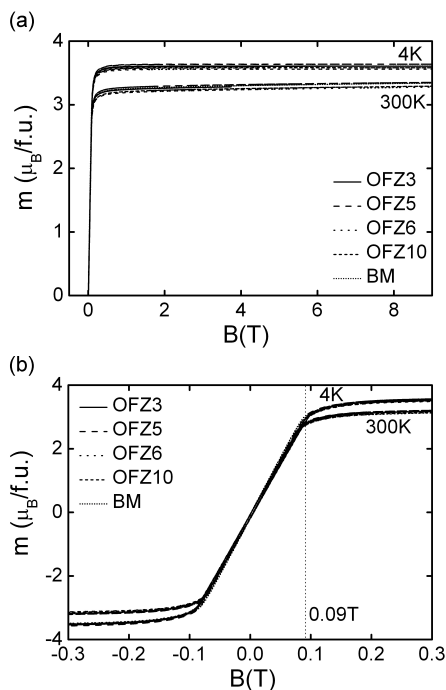


Figure 4: (a) Magnetization as a function of magnetic fields up to 9 T at $T = 4$ K and $T = 300$ K. All floating zone grown Cu_2MnAl samples, OFZ3, OFZ5, OFZ6, and OFZ10 as well as the Bridgman grown sample (BM) show the same behavior and saturate at $m \sim 3.6 \mu_B/\text{f.u.}$ and $m \sim 3.2 \mu_B/\text{f.u.}$ at $T = 4$ K and $T = 300$ K, respectively. (b) Magnetization as a function of magnetic fields for low fields. All samples saturate ferromagnetically above $B \geq 90$ mT. Data are not corrected for demagnetizing effects.

160 4. Single crystal neutron diffraction

161 In order to investigate the mosaic spread of the floating zone grown crystals,
 162 neutron scattering experiments at the single crystal diffractometer HEIDI [23]
 163 at FRM II were carried out. Neutrons with a wavelength of $\lambda = 0.87 \text{ \AA}$ (Cu-220
 164 monochromator) were used with a primary collimation of $30'$. Single crystals of
 165 different dimensions prepared from OFZ3, OFZ5, OFZ6 and OFZ10 (see Fig. 3)
 166 were investigated as well as a Bridgman grown (BM) single-crystalline plate
 167 with dimensions $20 \times 40 \times 3 \text{ mm}^3$.

168 For each crystal rocking scans with respect to the $\{400\}$ and $\{111\}$ lattice
 169 planes were carried out. For OFZ10 the $\{333\}$ lattice planes were studied and
 170 for BM a single (333) plane. Both the integrated and absolute intensities of the
 171 Bragg reflections of the different rocking scans vary because different sample
 172 volumes were measured for each direction. Nevertheless, the crystal mosaicity
 173 was obtained from the width of the rocking curves in terms of the full-width-
 174 have-maximum (FWHM) and taking into account the resolution function of the
 175 instrument [24].

176 An overview of the $\{400\}$ and $\{111\}$ Bragg scattering intensities as a function
 177 of the rocking angle ϕ is shown in Fig. 5. OFZ3 (a, b) and OFZ5 (c, d) show
 178 similar, highly homogeneously shaped rocking curves for all $\{400\}$ and $\{111\}$
 179 reflections. This is confirmed by the very homogeneous mosaic distribution
 180 around 0.25° for OFZ3 and OFZ5, respectively. In comparison, the accuracy
 181 of measurement was $\pm 0.05^\circ$. The mosaicities are summarized in Table 1. The
 182 rocking curves for OFZ6 (e, f) are slightly broadened due to a small second
 183 peak. This deviation also shows up in terms of the larger anisotropy of the
 184 mosaicity for the different scattering planes. Nevertheless, in comparison to
 185 the data reported for the Bridgman grown crystals, OFZ6 shows an essentially
 186 isotropic mosaic distribution.

187 Clear deviations from an isotropic mosaic spread are found for OFZ10 (g, h),
 188 where two intensity maxima are seen for most of the reflections. This signature
 189 is most likely due to the use of two different growth velocities (10 mm/h and
 190 5 mm/h) during the floating zone growth of OFZ10. This sensitivity of the
 191 mosaic distribution to variations of the growth rate might be advantageous
 192 when growing crystals with a given mosaic spread for use as polarizing neu-
 193 tron monochromators. As mentioned above, a mosaic spread ($0.2^\circ - 1.0^\circ$) is
 194 necessary for high neutron intensities.

195 Fig. 6 shows the rocking scan of the (111) plane of OFZ3 and the (333) plane
 196 of the large Bridgman grown sample. In comparison to the floating zone grown
 197 crystal, the rocking scan of the Bridgman grown crystal is less homogeneous and
 198 has a slightly larger mosaicity. The comparison shows that optical floating zone
 199 allows to reproducibly grow Cu_2MnAl single crystals with a *homogeneous* mosaic
 200 spread that is at least comparable to the mosaic spread of “good” Bridgman
 201 grown crystals.

Mosaicity \ Crystal	OFZ3	OFZ5	OFZ6	OFZ10	BM
(400)	0.25°	0.21°	0.48°	0.50°	
(040)	0.25°	0.22°	0.40°	0.30°	
(004)	0.22°	0.25°	0.29°	1.27°	
(111)	0.24°	0.23°	0.27°		
($\bar{1}\bar{1}\bar{1}$)	0.20°	0.22°	0.41°		
($1\bar{1}\bar{1}$)	0.25°	0.23°	0.31°		
($11\bar{1}$)	0.25°	0.27°	0.64°		
(333)	0.18°			0.73°	0.53°
($\bar{3}\bar{3}\bar{3}$)	0.21°			0.71°	
($3\bar{3}\bar{3}$)	0.26°			0.64°	
($3\bar{3}\bar{3}$)	0.27°			0.23°	

Table 1: Crystal mosaicities for different scattering planes of the floating zone (OFZ3, OFZ5, OFZ6 and OFZ10) and Bridgman grown (BM) Cu_2MnAl crystals. The mosaicities were calculated from the FWHM values of the Bragg peaks taking into account the instrumental resolution function [24]. The accuracy of the mosaicities is better than $\pm 0.05^\circ$.

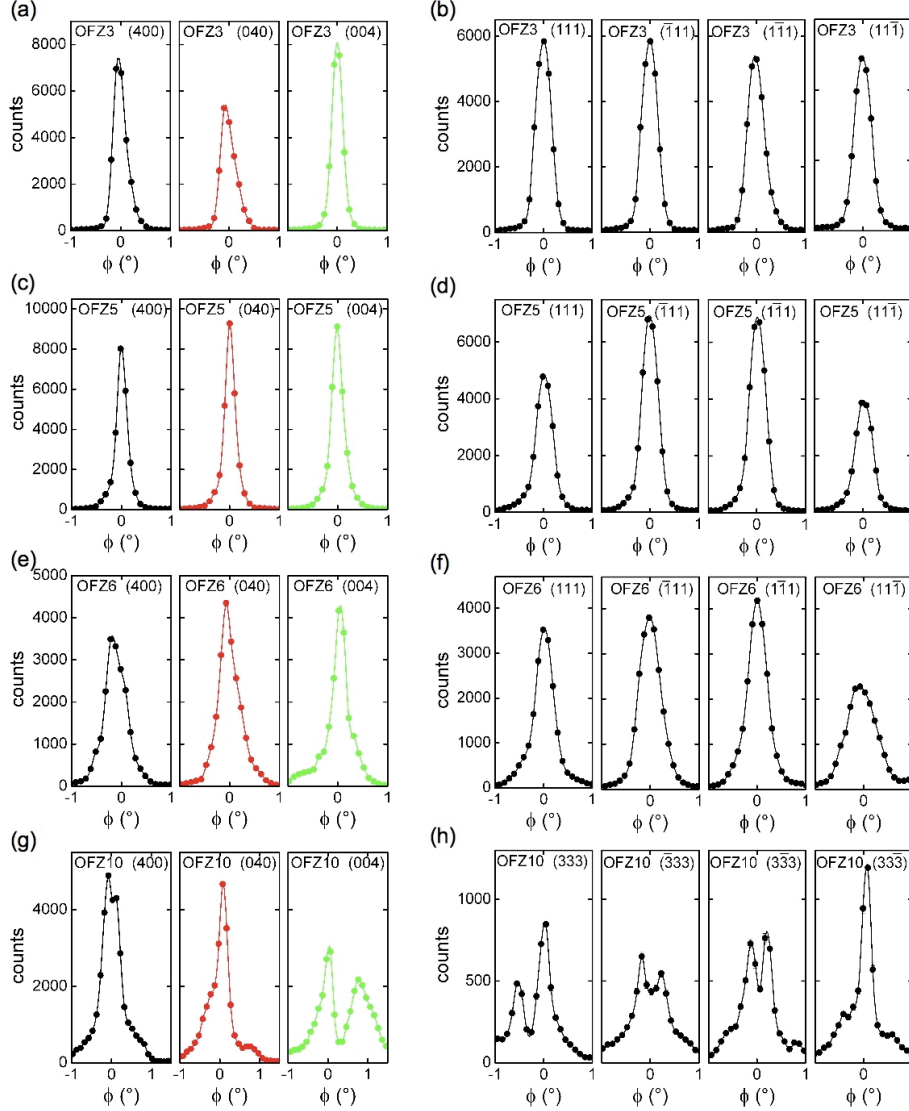


Figure 5: Overview of the $\{400\}$ and $\{111\}$ Bragg scattering intensities as a function of the rocking angle ϕ for the floating zone grown crystals. OFZ3 (a, b) and OFZ5 (c, d) show highly homogeneous shaped rocking curves for all $\{400\}$ and $\{111\}$ planes. For OFZ6 (e, f) the curves are slightly broadened. The inhomogeneous peak structure of crystal OFZ10 (g, h) is most likely due to a change of the growth rate during crystal growth. However, one has to take into consideration that the instrumental resolution for $\{333\}$ is better than for $\{111\}$ [24], leading to the more narrow peak structure in (h). The step width of the rocking scans was 0.1° .

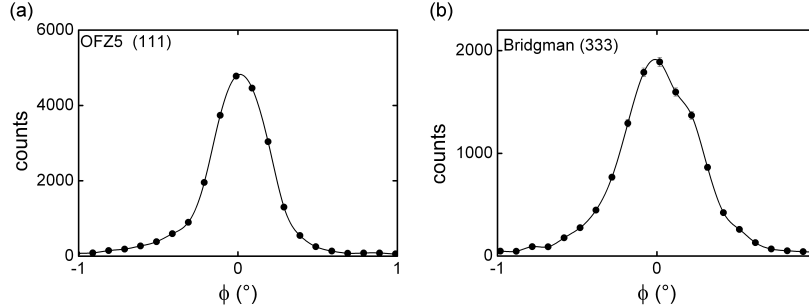


Figure 6: Comparison of the Bragg scattering intensities of OFZ5 (111) and the large Bridgman grown plate (333) as a function of the rocking angle ϕ . The rocking curve of the Bridgman crystal is slightly broadened, indicating a coarser mosaic spread in comparison with the floating zone grown crystal OFZ5.

202 5. Polarizing properties

203 We finally turn to the polarizing properties of the floating zone grown single
 204 crystals. As reported in the literature [9, 10], the Bragg (111) reflection of
 205 Cu_2MnAl may be used to generate a monochromatic beam of polarized neutrons.
 206 In general, scattering of an unpolarized neutron beam on a ferromagnet results in
 207 individual structure factors for nuclear F_{nuc} and magnetic F_{mag} scattering, that
 208 sum up individually to a common scattering intensity [25, 26]. For a ferromagnet
 209 the scattering intensity is given as

$$I \propto F_{\text{tot}}^2 = F_{\text{nuc}}^2 + q^2 F_{\text{mag}}^2, \quad (1)$$

210 where \mathbf{q} is the magnetic interaction vector and $q^2 = \sin^2 \alpha$. α is the angle be-
 211 tween the magnetization and the scattering vectors. For a cubic magnetic crys-
 212 tal without anisotropy, as it is the case for Cu_2MnAl , and in an unsaturated
 213 magnetic state q^2 takes a value of $2/3$.

214 For a saturated ferromagnet with the magnetization direction perpendicular
 215 to the scattering vector, q^2 takes a value of 1. In this case the scattering intensity
 216 for neutrons with spin parallel (+) to the magnetization direction is given as

$$I_+ \propto F_{\text{tot},+}^2 = F_{\text{nuc}}^2 + F_{\text{mag}}^2, \quad (2)$$

217 while

$$I_- \propto F_{\text{tot},-}^2 = F_{\text{nuc}}^2 - F_{\text{mag}}^2 \quad (3)$$

218 is the scattering intensity for neutrons with spin antiparallel (-) to the magne-
 219 tization direction.

220 In the case of Cu_2MnAl the magnetic structure factor for (111) Bragg scat-
 221 tering is comparable to the nuclear structure factor, i.e., $F_{\text{mag}}^{(111)} \simeq F_{\text{nuc}}^{(111)}$ [9].
 222 Considering Eq. 2 and Eq. 3, scattering of the (111) plane hence leads to a high

223 flipping ratio $R = I_+/I_-$ and a polarized neutron beam with a high polarization
 224 P defined as

$$P = \frac{I_+ - I_-}{I_+ + I_-}. \quad (4)$$

225 *5.0.1. Experimental set-up*

226 The measurements were carried out at the MIRA2 beamline at FRMII.
 227 The set-up used for polarization analysis is shown in Fig. 7 (a). An important
 228 prerequisite for polarization analysis is a continuous magnetic field along the
 229 flight path of the polarized neutrons since strong field gradients and especially
 230 zero field crossings lead to a depolarization of the neutron beam.

231 The cross section of the monochromatized neutron beam of wavelength
 232 $\lambda = 4.2 \pm 0.1 \text{ \AA}$ was determined by the source aperture (S1) and the sample aperture
 233 (S3). In this experiment the apertures were $S1 = 3 \times 4 \text{ mm}^2$ and $S3 = 5 \times 8 \text{ mm}^2$
 234 (width \times height), ensuring that the small samples were entirely illuminated by
 235 the neutron beam. A Be filter at a temperature of 30 K was used to remove
 236 neutrons with higher order wavelengths. The sample was positioned on a go-
 237 niometer in an external magnetic field. A magnetic guide field provided a con-
 238 tinuous magnetic field for the neutron beam after the (111) Bragg scattering at
 239 the sample.

240 The polarization of the neutron beam was analyzed with a ^3He cell that was
 241 provided by the HELIOS group of the FRMII [27]. The ^3He cell was placed
 242 inside a magnetic cavity that acts as a guide field. The cavity furthermore
 243 allowed to flip the polarization of the ^3He gas with an integrated adiabatic fast
 244 passage (AFP) flipper device [28]. A ^3He counter tube downstream of the cavity
 245 was used as a detector.

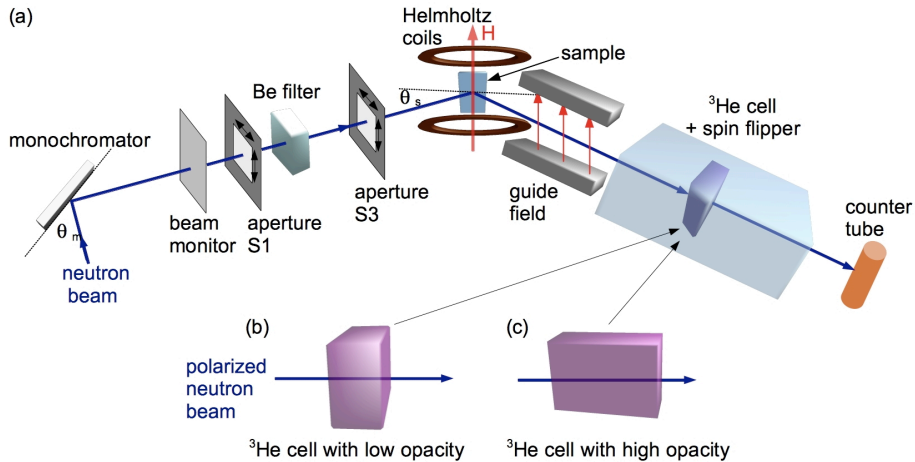


Figure 7: (a) Set-up for the polarization analysis of the Cu_2MnAl crystals at the MIRA2 beamline at FRMII. Details are given in the text. Arrangement of the ^3He cell (b) with low opacity and (c) with high opacity.

246 The polarization analysis was carried out with two different arrangements
 247 of the ^3He cell as shown in Fig. 7 (b, c). For the first set of measurements the
 248 ^3He cell was positioned perpendicular to the neutron beam. With this set-up
 249 the flight path of the neutrons through the polarized ^3He gas is short and the
 250 absorption is reduced, leading to a low opacity. In this configuration the ^3He
 251 cells had a polarization efficiency $P_0^{\text{rel}} \sim 80\text{-}85\%$ [29]. This only allows a relative
 252 measure of the polarization efficiency of the Cu_2MnAl crystals, but leads to good
 253 counting statistics and was therefore chosen to test the experimental set-up and
 254 record rocking scans and field dependencies. For an absolute measure of the
 255 polarization efficiency of the crystals, the ^3He cell was positioned parallel to the
 256 neutron beam. With this set-up the flight path of the neutrons through the
 257 polarized ^3He gas is long, hence leading to a high opacity. In this configuration
 258 the ^3He cells had a polarization efficiency of $P_0^{\text{abs}} > 99\%$ [29].

259 The samples grown in the image furnace (OFZ3, OFZ5, OFZ6 and OFZ10)
 260 and the small Bridgman grown sample (BMsmall) investigated were the same
 261 as those used for the magnetization measurements. These samples were small
 262 with dimensions of $5 \times 2.5 \times 2 \text{ mm}^3$. In addition, the large Bridgman grown
 263 (BM) crystal ($40 \times 20 \times 3 \text{ mm}^3$) that was characterized at HEIDI and a large
 264 inhomogeneously shaped slab (BMlarge, in average $60 \times 30 \times 4 \text{ mm}^3$), from which
 265 BMsmall was cut, were investigated. All samples were prepared and mounted
 266 with the large front side being a (111) plane.

267 In a first test the OFZ samples were mounted in a bespoke aluminum holder
 268 as shown in Fig. 8 (a). The holder was clamped within a horseshoe magnet where
 269 additional Fe pieces served as pole shoes. This set-up (without the Helmholtz
 270 coils) provided a magnetic field of $\sim 180 \text{ mT}$, which is twice the field necessary
 271 to saturate the samples (cf. Fig. 4).

272 However, measurements with this set-up resulted in unexpected low flipping
 273 ratios of $R \sim 2$. We believe that field gradients surrounding the sample lead
 274 to a depolarization of the beam right after the scattering process and, hence,
 275 to the low flipping ratios observed. Therefore, the set-up was changed. The
 276 horseshoe magnet and pole shoes were removed, and instead a homogeneous

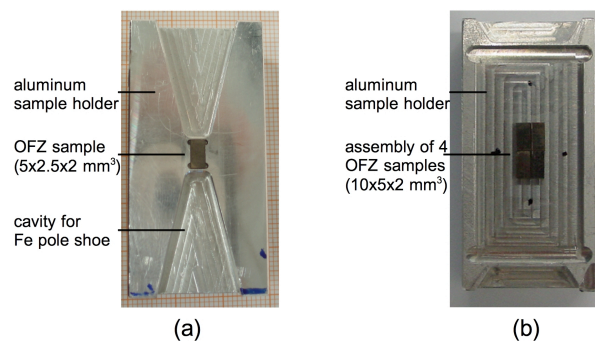


Figure 8: (a) Floating zone grown Cu_2MnAl sample mounted in a bespoke aluminum holder.
 (b) Assembly of four OFZ crystals as arranged for the polarization analysis.

277 magnetic field was generated by a set of Helmholtz coils as shown in Fig. 7 (a).
278 With the Helmholtz coils a magnetic field of up to 220 mT could be applied.

279 Rocking scans were recorded at a 2θ angle of 74.2° , appropriate for the
280 (111) Bragg reflex of a cubic crystal structure with lattice constant $a = 5.996 \text{ \AA}$
281 ($d_{(111)} = a/\sqrt{3}$) and a neutron wavelength $\lambda = 4.2 \text{ \AA}$. Typically the sample was
282 rocked through a range of 3° .

283 5.0.2. ^3He cell with low opacity

284 Rocking scans in an applied field of 220 mT were recorded analyzing both
285 spin configurations: the spin-up configuration (I_+ , Eq. 2), for which the ^3He cell
286 allows neutrons to pass with spin parallel to magnetization direction; and the
287 spin-down configuration (I_- , Eq. 3), for which the ^3He cell allows neutrons to
288 pass with spin antiparallel to the magnetization direction. In addition, rocking
289 scans with no applied field were recorded. The results for crystals OFZ3, OFZ5,
290 OFZ10 and BM are shown in Fig. 9. The curves are Gaussian fits to the data.

291 Similar to the results of the measurements at HEIDI, a narrow (111) Bragg
292 peak was observed for OFZ3 and OFZ5, as well as the double peak structure for
293 OFZ10 and the slightly broadened peak for the Bridgman grown sample (BM).
294 As expected from Eq. 1–3 the maximum intensity was obtained for the spin-up
295 configuration, the minimum intensity for the spin-down configuration and an
296 intensity maximum close to the spin-up configuration for the zero field mea-
297 surements. Analysis of the maximum intensities gives a flipping ratio $R \sim 4.5$
298 for OFZ3, OFZ5 and OFZ10 and a flipping ratio of $R \sim 10$ for the Bridgman
299 crystal.

300 Further, the field dependence of the maximum Bragg intensity of crystals
301 OFZ5 and BM, both for the spin-up and the spin-down configuration, was in-
302 vestigated. As shown in Fig. 10, the two crystals show different behavior. For
303 the large BM crystal both intensities remain at the same level for fields below
304 20 mT. With increasing field the spin-up intensity rises towards its maximum
305 value at around 40 mT and saturates. The spin-down intensity shows a strong
306 decrease above 20 mT and saturates at low intensities for fields above 40 mT.
307 This behavior is in agreement with Eq. 2 and Eq. 3, if a ferromagnetic saturation
308 of the sample around 40 mT is assumed. This is plausible due to its elongated
309 form and, hence, reduced demagnetization factor compared to the OFZ crystals.
310 The slight decrease of both intensities at the highest fields may be caused by
311 inhomogeneous field distributions around the crystals.

312 Different behavior is observed for the floating zone grown crystal OFZ5 (see
313 Fig. 10 (b)). Here spin-up and spin-down intensities start at similar intensities
314 at zero field. With increasing fields up to 75 mT both intensities slightly de-
315 crease. At 75 mT the curves split and show a curved increase (spin-up) and
316 decrease (spin-down) to higher fields. No clear saturation is observed for fields
317 up to 220 mT. This behavior is in stark contrast to what was expected from the
318 magnetization curves (cf. Fig. 4). At a field of 90 mT both the spin-up and spin-
319 down intensities were expected to saturate. We believe that the small sample
320 dimension is responsible for the unconventional field dependence of the intensi-
321 ties and, hence, for the low flipping ratio. The geometry of the sample might

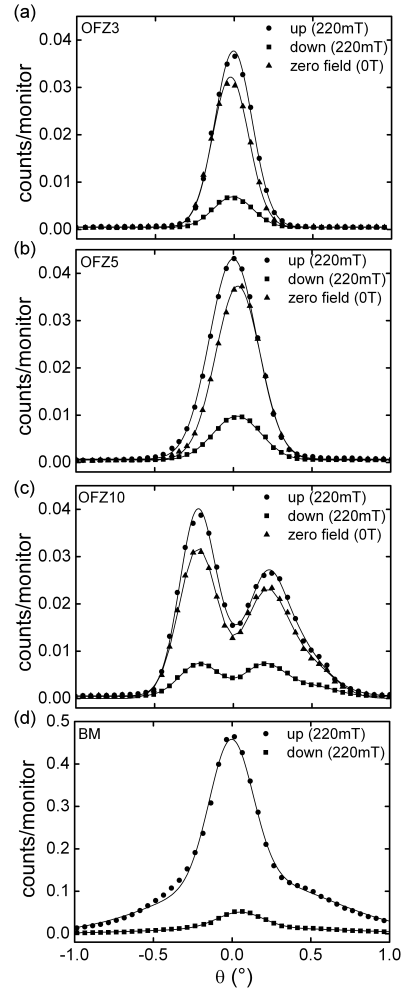


Figure 9: Rocking scans at the (111) Bragg reflexion of floating zone grown crystals OFZ3, OFZ5 and OFZ10 and of the Bridgman grown crystal (BM) with the ^3He cell perpendicular to the neutron beam. Measurements were taken in spin-up (I_+) and spin-down (I_-) configuration in an external field of 220 mT and in zero field for the OFZ crystals. The intensities are normalized to counts per monitor values. Note that the intensities for the large BM crystal are around 10 times larger than those for the small OFZ crystals.

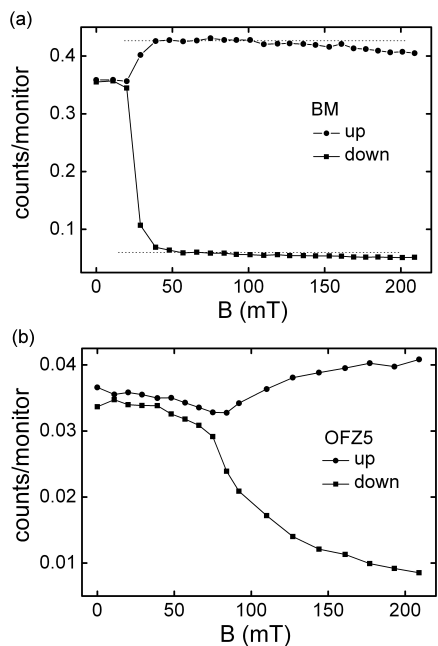


Figure 10: Field dependence of the Bragg peak maximum for the spin-up and the spin-down configuration. (a) For the large Bridgman grown crystal the intensities for both spin configurations start at a similar value, split step-like at a field above 20 mT and saturate at fields exceeding 40 mT. (b) Different behavior is observed for the floating zone grown crystal OFZ5. With increasing field both intensities slightly decrease and split for fields above 75 mT. The splitting is gradual with no clear saturation up to a field of 220 mT.

322 reduce the magnetic polarization of the sample and generate inhomogeneous
 323 field distributions inside and outside the sample that depolarize the scattered
 324 neutrons.

325 5.0.3. ^3He cell with high opacity

326 In order to measure the absolute polarization, the last set of data was taken
 327 with the ^3He cell parallel to the neutron beam (see Fig. 7 (c)). The intensity at
 328 the maximum Bragg peak positions of each sample for both spin-up and spin-
 329 down configuration was recorded as well as the background. The measurement
 330 times were increased in order to obtain good counting statistics. The resulting
 331 flipping ratios and polarization efficiencies are shown in Table 2. A low po-
 332 larization efficiency of $P \sim 80\%$ for the small floating zone grown crystals was
 333 obtained as compared to the very good $P \sim 97\%$ for the large Bridgman grown
 334 crystal.

335 5.0.4. Role of sample geometry

336 In order to investigate the influence of the sample geometry on the polar-
 337 ization efficiency two independent measurements were performed. First, a large

CRYSTAL	OFZ3	OFZ5	OFZ6	OFZ10	BM
Sample dimension (mm ³)	5 × 2.5 × 2	5 × 2.5 × 2	5 × 2.5 × 2	5 × 2.5 × 2	40 × 20 × 3
Flipping ratio R	8.6	8.3	8.1	9.8/5.2	60.3
Polarization efficiency P (%)	79	79	78	81/68	97

Table 2: Sample dimensions, flipping ratios and polarization efficiencies for the small floating zone crystals (OFZ) and the large Bridgman grown crystal (BM).

338 Bridgman grown sample (BMlarge) and a small sample (BMsmall) prepared
 339 from BMlarge with dimensions similar to the OFZ crystals were examined. As
 340 a second test an assembly of the floating zone crystals OFZ3, OFZ5, OFZ6 and
 341 OFZ10, as shown in Fig. 8 (b), was measured.

342 From the first measurements we obtained a flipping ratio $R = 33$ for BMlarge
 343 in comparison to $R = 8.2$ for BMsmall. The flipping ratio $R = 8.2$ for the small
 344 Bridgman grown sample is similar to the low value obtained for the small floating
 345 zone grown crystals.

346 The rocking scan of the assembly, as the second test, is shown in Fig. 11.
 347 The rocking curve shows a clear double peak structure that results from a slight
 348 misalignment of the (111) planes of each crystal. Nevertheless, the flipping
 349 ratios of each of the two Bragg peaks are 23 and 20 (see Table 3).

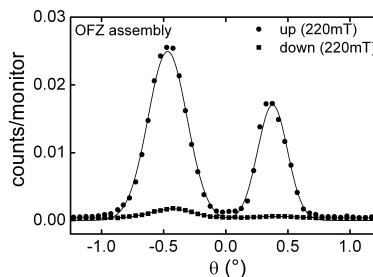


Figure 11: Rocking scan of the assembly of floating zone crystals OFZ3, OFZ5, OFZ6 and OFZ10 for both spin-up and spin-down configuration. Misalignment of the (111) planes of each crystal with respect to each other leads to the double peak structure. The assembly shows increased flipping ratios of $R = 23$ and $R = 20$ for each of the two Bragg peaks compared to $R \sim 8$ for each OFZ sample by itself.

350 The increase of the flipping ratios from $R \sim 8$ of each OFZ sample by itself
 351 to $R \sim 20$ for an assembly of the same samples and the reduced flipping ratio
 352 $R = 8.2$ of the small Bridgman sample compared to $R = 33$ of the large Bridgman
 353 sample clearly identify the sample dimension as the origin of the low flipping
 354 ratios and polarization efficiencies of the floating zone grown crystals. Since
 355 the small floating zone crystals and the small Bridgman sample show a similar
 356 flipping ratio $R \sim 8$, the floating zone grown crystals are expected to achieve

357 high polarization efficiencies comparable to those obtained for Bridgman grown
 358 crystals if the problems that arise due to the sample geometry are avoided. This
 359 may be achieved by growing larger crystals, by an assembly of several samples,
 360 or by a suppression of the stray fields or field inhomogeneities by embedding
 361 the Cu_2MnAl crystals in an adequate ferromagnetic material.

CRYSTAL	OFZ ASSEMBLY	BM LARGE	BM SMALL
Sample dimension (mm^3)	$10 \times 4 \times 2$	$\sim 60 \times 30 \times 4$	$5 \times 2.4 \times 1.8$
Flipping ratio R	23/20	33	8.2
Polarization efficiency $P(\%)$	92/90	94	79

Table 3: Sample dimensions, flipping ratios and polarization efficiencies of Cu_2MnAl samples OFZassembly, BMlarge and BMsmall additionally measured at MIRA in order to analyze the dependence of the polarization efficiency on the sample geometry.

362 6. Conclusion

363 In summary eight single crystals of the Heusler compound Cu_2MnAl were
 364 grown by crucible-free floating zone: two in a vertical double ellipsoid image fur-
 365 nace at IFW Dresden and six with a UHV-compatible image furnace at TUM.
 366 We found that Cu_2MnAl shows a strong tendency to crystallize in the cubic
 367 $L2_1$ crystal structure, indicating a congruent melting formation. The temper-
 368 ature gradient of the image furnace seems to be large enough to avoid the
 369 decomposition of Cu_2MnAl . The high purity static inert gas environment in
 370 the UHV-compatible image furnace at TUM was indispensable to reduce the
 371 oxygen formation around the molten zone. High purity conditions allowed to
 372 establish stable growth conditions and, hence, to obtain single crystals across
 373 the entire diameter for each of the six crystals grown with the image furnace at
 374 TUM. No preferred growth direction of the floating zone grown crystals could
 375 be identified.

376 Comparison of the magnetic properties of four crystals established a repro-
 377 ducible magnetic moment of $m \sim 3.6 \mu_{\text{B}}/\text{f.u.}$ at 4 K and $m \sim 3.2 \mu_{\text{B}}/\text{f.u.}$ at
 378 300 K for each crystal (within 3%). This is in perfect agreement with the mag-
 379 netic moments measured for a Bridgman grown crystal and those reported in
 380 literature [7].

381 Neutron diffraction of the $\{400\}$ and $\{111\}$ Bragg intensities established an
 382 isotropic mosaic spread of the floating zone grown crystals when constant growth
 383 parameters were applied. This is a clear advantage compared to Bridgman
 384 grown crystals where an anisotropic mosaic spread is reported [12].

385 Further, a study of the polarizing properties was performed. For a large
 386 Bridgman grown crystal a high polarization efficiency of 97% was found. The

387 lower polarization efficiency of the floating zone grown crystals was found to be
388 due to their small sample dimensions and could be raised to 91% by an assembly
389 of four small crystals.

390 In conclusion, single crystal growth of Cu_2MnAl with optical floating zone
391 allows to reproducibly grow crystals with a homogeneous mosaic distribution.
392 This avoids the main drawback of the Bridgman grown crystals [12]. For com-
393 mercial applications it will be necessary to grow single crystals with a larger
394 diameter. Moreover, a seed with a predefined orientation may allow to prepare
395 larger samples with a (111) plane from the crystals grown. Actually, recent
396 growth experiments already allowed the successful growth of oriented Cu_2MnAl
397 single crystals with a diameter of up to 10 mm [30]. Since the size of polarizing
398 crystals typically used for technical applications in neutron scattering starts at
399 around $10 \times 20 \text{ mm}^2$ [31], we believe that in future investigations these dimen-
400 sions should be accessible with floating zone crystal growth.

401 **Acknowledgments**

402 We gratefully acknowledge support and discussions with S. Masalovitch,
403 B. Russ, T. Adams, S. Mühlbauer, N. Vizont, J. Repper, A. Mantwill, R.
404 Schwikowski, the team of the crystal laboratory at TUM, and the team of FRM
405 II. We also gratefully acknowledge financial support through the DFG collabo-
406 rative research network TRR80 (From electronic correlations to functionality),
407 the DFG research unit FOR960 (quantum phase transitions) and individual
408 grants under contract PF393/10 and PF393/11.

409 **References**

- 410 [1] S. Chadov, X. Qi, J. Kübler, G. H. Fecher, C. Felser, and S.-C. Zhang,
411 *Nature Materials* **9**, 541 (2010).
- 412 [2] T. Graf, C. Felser, and S. S. Parkin, *Progress in Solid State Chemistry* **39**,
413 1-50 (2011).
- 414 [3] C. Felser and B. Hillebrands, *Journal of Physics D Applied Physics* **42**,
415 080301 (2009).
- 416 [4] D. Sprungmann, K. Westerholt, H. Zabel, M. Weides, and H. Kohlstedt,
417 *Physical Review B* **82**, 060505 (2010).
- 418 [5] D. Erb, G. Nowak, K. Westerholt, and H. Zabel, *Journal of Physics D:*
419 *Applied Physics* **43**, 285001 (2010).
- 420 [6] F. Heusler, *Verhandlungen der Deutschen Physikalischen Gesellschaft* **5**
421 (1903).
- 422 [7] B. Michelutti, *Solid State Communications* **25**, 163 (1978).

- 423 [8] W. G. Williams, *Polarized neutrons* (Clarendon Press, Oxford, New York,
424 1988).
- 425 [9] A. Delapalme, J. Schweizer, G. Couderchon, and R. P. de la Bathie, *Nuclear
426 Instruments and Methods* **95**, 589 (1971).
- 427 [10] A. Freund, R. Pynn, W. Stirling, and C. Zeyen, *Physica B&C* **120**, 86
428 (1983).
- 429 [11] A. K. Freund, *Journal of Applied Crystallography* **42**, 36-42 (2009).
- 430 [12] P. Courtois, *Physica B: Condensed Matter* **267-268**, 363 (1999).
- 431 [13] P. Courtois, B. Hamelin, and K. H. Andersen, *Nuclear Instruments and
432 Methods in Physics Research Section A: Accelerators, Spectrometers, De-
433 tectors and Associated Equipment* **529**, 157 (2004).
- 434 [14] A. Neubauer, J. Boeuf, A. Bauer, B. Russ, H. v. Löhneysen, and C. Pfei-
435 derer, *Review of Scientific Instruments* **82**, 013902 (2011).
- 436 [15] W. Köster and T. Gödecke, *Zeitschrift für Metallkunde* **57**, 889 (1966).
- 437 [16] B. Dubois and D. Cheverau, *Journal of Materials Science* **14**, 2296 (1979).
- 438 [17] Y. Sakka and M. Nakamura, *Journal of Materials Science* **25**, 2549 (1990).
- 439 [18] R. Kainuma, N. Satoh, X. J. Liu, I. Ohnuma, and K. Ishida, *Journal of
440 Alloys and Compounds* **266**, 191 (1998).
- 441 [19] Seed and feed rods for crystals HKZ363, OFZ1, OFZ3, OFZ4 and OFZ5
442 were all prepared in the rod-casting furnace at the IFW Dresden from
443 the same batch of Bridgman grown Cu_2MnAl single crystals. The seed and
444 feed rods for crystals OFZ6 and OFZ10 were prepared from pure starting
445 material in the rod-casting furnace at TUM.
- 446 [20] A. Neubauer, Ph.D. thesis, Technische Universität München (2011).
- 447 [21] W. Münzer, Diploma thesis, Technische Universität München (2009).
- 448 [22] A. Bauer, Diploma thesis, Technische Universität München (2009).
- 449 [23] M. Meven, V. Hutanu, and G. Heger, *Neutron News* **18**, 19 (2007).
- 450 [24] The FWHM values were obtained by means of the measurement software at
451 HEIDI through linear interpolation of the measured intensities. The steep
452 edge and the small statistical error of the supporting points in the peak area
453 give $\pm 0.05^\circ$ as a pessimistic assumption of the instrumental error (due to
454 the step width of 0.1°). The instrumental resolution function depends on
455 the diffraction angle 2θ , giving a beam divergence of around 0.13° for {400},
456 around 0.11 for {333}, and around 0.34° for the {111} scattering planes.
457 The crystal mosaicities were then obtained via the relation: $(\text{mosaicity})^2 =$
458 $(\text{FWHM})^2 - (\text{beam divergence})^2$.

- 459 [25] G. E. Bacon and K. Lonsdale, *Reports on Progress in Physics* **16**, 1 (1953).
- 460 [26] P. J. Webster, *Contemporary Physics* **10**, 559 (1969).
- 461 [27] [http://www.frm2.tum.de/en/science/service-groups/neutrons-optics/3he-](http://www.frm2.tum.de/en/science/service-groups/neutrons-optics/3he-polarizer-helios)
462 [polarizer-helios](http://www.frm2.tum.de/en/science/service-groups/neutrons-optics/3he-polarizer-helios), 2010.
- 463 [28] E. Babcock, A. Petoukhov, J. Chastagnier, D. Jullien, E. Lelièvre-Berna,
464 K. Andersen, R. Georgii, S. Masalovich, S. Boag, C. Frost, et al., *Physica*
465 *B: Condensed Matter* **397**, 172 (2007).
- 466 [29] Sergey Masalovitch, personal communication, 2010.
- 467 [30] A. Bauer, C. Pfeiderer, unpublished.
- 468 [31] Peter Böni, personal communication, 2010.